This is a repository copy of *Optimising dopants and properties in BiMeO3 (Me = Al, Ga, Sc, Y, Mg2/3Nb1/3, Zn2/3Nb1/3, Zn1/2Ti1/2) lead-free BaTiO3-BiFeO3 based ceramics for actuator applications*.

White Rose Research Online URL for this paper:
http://eprints.whiterose.ac.uk/131641/

Version: Accepted Version

Optimising dopants and properties in BiMeO$_3$ (Me = Al, Ga, Sc, Y, Mg$_{2/3}$Nb$_{1/3}$, Zn$_{2/3}$Nb$_{1/3}$, Zn$_{1/2}$Ti$_{1/2}$) lead-free BaTiO$_3$-BiFeO$_3$ based ceramics for actuator applications

Shunsuke Murakami[1], Nihal Thafeem Ahmed Faheem Ahmed[1], Dawei Wang[1], Antonio Feteira[2], Derek C. Sinclair[1], and Ian M Reaney[1, *]

[1]Department of Materials Science and Engineering, University of Sheffield, Sheffield S1 3JD, UK

[2]Materials Engineering and Research Institute, Sheffield Hallam University, Sheffield S1 1WB, UK

*Corresponding Author Prof. Ian M Reaney: i.m.reaney@sheffield.ac.uk

Abstract

A crystallochemical framework is proposed based on electronegativity difference (e_n) and tolerance factor (t) to optimise the BiMeO$_3$ dopants and therefore the piezoelectric and high-field strain response in BaTiO$_3$-BiFeO$_3$ based ceramics. Compositions in the series 0.05Bi(Me)O$_3$-0.25BaTiO$_3$-0.7BiFeO$_3$ (BMe-BT-BF, Me: Y, Sc$_{1/2}$Y$_{1/2}$, Mg$_{2/3}$Nb$_{1/3}$, Sc, Zn$_{2/3}$Nb$_{1/3}$, Zn$_{1/2}$Ti$_{1/2}$, Ga, and Al) were fabricated using solid state synthesis and furnace cooled. Scanning electron microscopy and X-ray diffraction revealed that only Bi(Mg$_{2/3}$Nb$_{1/3}$)O$_3$ and BiScO$_3$ dopants, which lie in a narrow range of e_n vs. t, form homogeneous ceramics, free from secondary phases reflected in their superior piezoelectric coefficients (d_{33} ~145 pC/N). All other BiMeO$_3$ additions exhibited either secondary phases (Y) and/or promoted a two-phase perovskite matrix (Zn, Ga and Al). The promising initial properties of BiScO$_3$ doped compositions prompted further studies on 0.05BiScO$_3$-(0.95-x)BaTiO$_3$-(x)BiFeO$_3$ (BS-BT-BF, x = 0.55, 0.60, 0.625, 0.65, and 0.70) ceramics. As x increased the structure changed from predominantly pseudocubic to rhombohedral, resulting in a transition from a relaxor-like to ferroelectric response. The largest d_{33}^* (465 pm/V) was achieved for x = 0.625 under 5 kV/mm at the crossover from relaxor to ferroelectric behaviour. BS-BT-BF with x = 0.625 showed >0.3% strain under 6 kV/mm up to 175ºC, demonstrating its potential for actuator applications.

1. **Introduction**

Pb(Zr,Ti)O$_3$ (PZT) has been widely used in piezoelectric devices over the past few decades because of its excellent piezoelectric performance and temperature reliability [1, 2]. However, concerns about environment and health issues have been growing due to the toxicity of lead [3, 4] and many researchers have attempted to find alternative lead-free

materials.

The majority of lead-free piezoelectric materials reported so far are based on (K,Na)NbO₃ (KNN), Na$_{1/2}$Bi$_{1/2}$TiO₃ (NBT), and (Ba,Ca)(Zr,Ti)O₃ (BCZT). KNN based materials nominally have a high T$_C$ and high piezoelectric coefficient (d_{33} >300 pC/N) [2] but they exhibit a temperature dependence from room temperature (RT) to 100ºC [5-9]. NBT based materials undergo depolarization at relative low temperatures (~150ºC) and are highly hysteretic for compositions with high strain (>0.35%) [10]. BCTZ based materials show high piezoelectric performances at the expense of a low Curie temperature (T_C) (<100ºC) [11, 12].

In contrast, BaTiO₃-BiFeO₃ (BT-BF) based ceramics have been reported to have high piezoelectric coefficient, d_{33} = 402 pC/N and high T_C = 454ºC after quenching [13]. Myang Hwan Lee et al. [13] reported that quenched 0.67Bi$_{1.05}$(Fe$_{0.97}$Ga$_{0.03}$)O₃-0.33BaTiO₃ lies on a morphotropic phase boundary (MPB) between tetragonal and rhombohedral structures and as a result they claimed to have achieved the highest d_{33}. Although there are significant challenges to apply quenching for the industrial fabrication of high strain actuators, this result shows the potential of BT-BF ceramics for piezoelectric applications.

Many researchers have pointed out the drawbacks of a BiFeO₃ containing system for high field applications in which, either the loss for Bi or the formation of mixed valence Fe ions results in large leakage currents [14-30] but various dopants have been shown to alleviate these problems. Rare earth ions are reported to substitute on the A site of BiFeO₃ and improve d_{33} but there are conflicting reports as to whether they improve breakdown strength/d_{33} of BT-BF ceramics [23-29]. Most dopants reported to improve the resistivity and enhance piezoelectric activity reside on the B-site of BiFeO₃ [14-22]. In BT-BF ceramics, many researchers suggest that dopants should be chosen to enhance tetragonality [13, 14, 16] Zhou et al. [14] reported that Al^{3+} promotes the coexistence of rhombohedral and orthorhombic phases in 0.725BiFe$_{1-x}$Al$_x$O₃-0.275BaTiO₃ + 1 mol% MnO₂ ceramics (x = 0.01-0.03) and improves d_{33} from 126 pC/N (x = 0) to 138 pC/N (x = 0.02). Zhou et al. [19] reported that for 0.71BiFe$_{1-x}$(Ni$_{1/2}$Ti$_{1/2}$)$_x$O₃-0.29BaTiO₃ (x = 0-0.09) + 0.6 wt% MnO₂ ceramics, the lattice parameter of the pseudocubic structure increases as x increases and that x = 0.03 showed the highest d_{33} = 156 pC/N. On the other hand, Luo et al. [30] reported the piezoelectric properties for both A and B site doped BT-BF, (0.75-x)BiFeO₃-0.25BaTiO₃-xLa(Co$_{0.5}$Mn$_{0.5}$)O₃ + 1 mol% MnO₂ ceramics, which they reported to show an MPB of rhombohedral and orthorhombic structures (0.01≤x≤0.03) with d_{33} ~108 pC/N (x =0.02). As evidenced in the brief literature presented above, doped BT-BF ceramics exhibit the coexistence of crystal structures, which are

reputed to give rise to a large piezoelectric response but there are no crystallochemical trends that have been shown to predict the optimum dopant type in BT-BF ceramics. The most comprehensive study to date by Zheng *et al.* [22] investigated the piezoelectric properties for $0.70Bi_{1.05}Fe_{0.97}A_{0.03}O_3-0.30BaTiO_3$ (A: Sc, Ga, Al, In, Ni, Co) ceramics and reported the ceramics with Sc, Ga, and Al showed good d_{33} (160-180 pC/N) but piezoelectric properties by Zheng *et al.* [22] were optimised with a quenching technique and do not relate to conventional furnace cooled ceramic which have far greater potential industrial scale-up. There is still therefore, a need to synthesise and investigate non-quenched BF-BT ceramics with high strain/piezoelectric performance but it is clear from previous studies that the most suitable dopants need to be determined.

Ideally, for optimised properties in doped BT-BF ceramics, universal design rules are required based on established crystallochemical principles. The tolerance factor (*t*) is known to indicate the local strain and stability of a perovskite phase. It has been used many times to predict/explain properties. It is defined as:

$$t = \frac{r_A + r_O}{\sqrt{2}(r_B + r_O)}$$

where r_A, r_B, r_O denote the radius of the A-site, B-site and oxygen ion, respectively [1, 32]. When the tolerance factor of a crystal is close to 1.0, the crystal structure is more stable and given a matrix composed of highly polarisable ionic species, ferroelectric properties are encouraged. Electronegativity difference, e_n, can also indicate the stability of the crystal structure, approximates the ionicity/covalency of the bonding and is expressed as:

$$e_n = \frac{X_{a-o} + X_{b-o}}{2}$$

where X_{a-o} is the difference between the electronegativity of the A ion and the oxygen ion, X_{b-o} is the difference between the electronegativity of the B ion and the oxygen ion. When e_n is large, the bonding energy between the cation and oxygen ion increases and the crystal structure becomes more stable [33, 34]. These two crystallochemical factors, listed in Table 1 (Table 2 shows the relevant ionic radii and electronegativity values) for the studied composition, have been used in many ferroelectric systems but not brought to bear in BT-BF. To study the role of e_n and t in determining the optimum dopants for BF-BT ceramics, compositions in the series $0.05Bi(Me)O_3-(0.95-x)BaTiO_3-(x)BiFeO_3$ (Me: Y, $Sc_{1/2}Y_{1/2}$, $Mg_{2/3}Nb_{1/3}$, Sc, $Zn_{2/3}Nb_{1/3}$, $Zn_{1/2}Ti_{1/2}$, Ga, Al, x = 0.70) were systematically investigated. x = 0.70 was nominally chosen to determine the phase equilibria in furnace cooled samples as a function of e_n and t and not with the intention of optimising properties for each composition.

However, once ideal dopants were identified, e.g. $Mg_{2/3}Nb_{1/3}$ and Sc, optimisation of strain was carried out by varying the composition in $BiScO_3$ doped ceramics a function of x. We comment that $Mg_{2/3}Nb_{1/3}$ doped ceramics are the focus of a separate paper by the same authors in which optimisation of strain (0.4%) and high $d_{33}{}^*$ was also demonstrated [31].

Table 1. Tolerance factor and electronegativity difference for $Bi(Me)O_3$ (Me = Y, $Sc_{1/2}Y_{1/2}$, $Mg_{2/3}Nb_{1/3}$, Sc, $Zn_{2/3}Nb_{1/3}$, $Zn_{1/2}Ti_{1/2}$, Ga, Al) and $BiFeO_3$.

$Bi(Me)O_3$	Tolerance factor (t)	Electroneg. difference (e_n)
$BiYO_3$	0.845	1.82
$Bi(Sc_{1/2}Y_{1/2})O_3$	0.876	1.79
$BiScO_3$	0.907	1.75
$Bi(Zn_{2/3}Nb_{1/3})O_3$	0.922	1.62
$Bi(Mg_{2/3}Nb_{1/3})O_3$	0.930	1.73
$Bi(Zn_{1/2}Ti_{1/2})O_3$	0.939	1.63
$BiGaO_3$	0.963	1.53
$BiAlO_3$	1.005	1.63
$BiFeO_3$	0.951	1.52

Table 2. Ion radius and electronegativity for Bi^{3+}, Fe^{3+}, Ba^{2+}, Ti^{4+}, Y^{3+}, Sc^{3+}, Mg^{2+}, Nb^{5+}, Zn^{2+}, Ga^{3+}, Al^{3+}, O^{2-}.

Ion	Ion radius (nm)	Electronegativity
Bi^{3+}	1.35	2.02
Fe^{3+}	0.645	1.83
Ba^{2+}	1.61	0.89
Ti^{4+}	0.605	1.54
Y^{3+}	0.900	1.22
Sc^{3+}	0.745	1.36
Mg^{2+}	0.720	1.31
Nb^{5+}	0.640	1.60

Zn^{2+}	0.740	1.65
Ga^{3+}	0.620	1.81
Al^{3+}	0.535	1.61
O^{2-}	1.40	3.44

2. Experimental procedure

$0.05Bi(Me)O_3$-$(0.95-x)BaTiO_3$-$xBiFeO_3$ (Me: Y, $Sc_{1/2}Y_{1/2}$, $Mg_{2/3}Nb_{1/3}$, Sc, $Zn_{2/3}Nb_{1/3}$, $Zn_{1/2}Ti_{1/2}$, Ga, Al, x =0.55, 0.60, 0.625, 0.65, 0.70) ceramics were prepared by conventional solid-state methods. The starting raw materials were as follows; Bi_2O_3 (99.9%, Acros Organics), Fe_2O_3 (99%, Sigma Aldrich), $BaCO_3$ (99%, Sigma Aldrich), TiO_2 (99.9%, Sigma Aldrich),Y_2O_3 (99.99%, Alfa Aesar), Sc_2O_3 (99.995%, Stanford Materials), MgO(99%, Sigma Aldrich), Nb_2O_5 (99.5%, Alfa Aesar), ZnO(99.9%, Sigma Aldrich), Ga_2O_3(99.99%, Stanford Materials), Al_2O_3(99.8%, Aldrich Chemical Company). The raw materials were dried overnight to eliminate moisture, hydroxide, and adsorbed CO_2 before weighing. The dried powders were weighed and attrition milled for 1 to 2 h at 300 rpm in a Union Processes attritor mill (Szegvari Attritor System, Union Process), using 3 mm diameter yttria-stabilised zirconia media in isopropanol. The slurry was separated from the media and dried overnight at 80 ºC. The mixed dried powder was calcined 2 h at 800 ºC in Al_2O_3 crucible in a muffle furnace. The calcined powder was further attrition milled and dried as mentioned above. The attrition milled powder was mixed with poly(vinyl alcohol) equal to 0.5 wt% of the attrition milled powder, dried, pulverized by using an agate pestle and mortar, and sieved through a 250 micron mesh. ~0.3 g batches of powder were uniaxially pressed into discs with diameter of 10 mm at 125 MPa to form green body pellets. These compacts were sintered 2 h between 940 to 1020 ºC after burning out the binder at 550 ºC. Sintering temperatures and relative densities of the ceramics are shown in Table 3. To evaluate the electric, dielectric, and piezoelectric properties of the samples, silver paste electrodes were applied to the sintered pellets, and then fired 2h at 500 ºC.

To measure X-ray powder diffraction (XRD), the sintered pellets were crushed and ground to fine powder. XRD was performed using a Bruker D2 phaser X-ray diffractometer (Bruker) with Cu$K\alpha$ radiation. The microstructure of polished pellets were studied using a scanning electron microscope (SEM) equipped with a backscattered electron detector (BSE) (Phillips, XL30). The surfaces of the samples were ground and mirror polished using wet abrasive paper. Samples were further polished using diamond abrasives in a water-based lubricant (MetPrep Ltd.).

The relative permittivity (ε_r) and dielectric loss (tanδ), were measured at 10 kHz using an LCR meter (HP, 4284A) for comparison between all samples. The temperature dependence of the ε_r and tanδ from 1-250 kHz were measured in the temperature range of 20 to 700ºC for selected samples. Polarisation-Electric field (*PE*) hysteresis loops and electric field-induced strain (SE) curves were measured at 1 Hz up to 7 kV/cm from room temperature to 175ºC in silicone oil using a ferroelectric tester (AixACCT, TF 2000). The impedance was measured from 100 to 500ºC in the frequency range 20 Hz to 1 MHz using a Precision LCR Meter (Agilent, E4980A). d_{33} was measured with a piezoelectric meter (PiezoMeter System, PIEZOTEST) shortly after poling. The poling treatment was conducted in silicone oil at 90ºC under dc field at 40 to 50 kV/cm for 20 minutes.

Table 3. Sintering temperature and relative density for $0.05Bi(Me)O_3$-$(0.95$-$x)BaTiO_3$-$xBiFeO_3$ (*Me*: Y, $Sc_{1/2}Y_{1/2}$, $Mg_{2/3}Nb_{1/3}$, Sc, $Zn_{2/3}Nb_{1/3}$, $Zn_{1/2}Ti_{1/2}$, Ga, Al, x =0.55, 0.60, 0.625, 0.65, 0.70) ceramics

Composition	Sintering temperature (°C)	Relative density (%)
$Bi(Me)O3$-$0.25BaTiO3$-$0.70BiFeO3$		
Me = Y	920	94.9
Me = $Sc_{1/2}Y_{1/2}$	940	95.7
Me = $Mg_{2/3}Nb_{1/3}$	1000	96.8
Me = $Zn_{2/3}Nb_{1/3}$	1010	97.4
Me = $Zn_{1/2}Ti_{1/2}$	1010	96.9
Me = Ga	990	94.9
Me = Al	980	96.0
Me = Sc		
$(0.05BiScO_3$-$(1$-$x)BaTiO_3$-$(x)BiFeO_3)$		
x = 0.55	1020	97.4
x = 0.60	1005	94.0
x = 0.625	990	98.0
x = 0.65	1010	92.8
x = 0.70	1010	93.8

3. Results and discussion
3.1 XRD analysis and microstructure

XRD diffractograms of $0.05Bi(Me)O_3$-$0.70BaTiO_3$-$0.25BiFeO_3$ (*Me*: Y, $Sc_{1/2}Y_{1/2}$, $Mg_{2/3}Nb_{1/3}$, Sc, $Zn_{2/3}Nb_{1/3}$, $Zn_{1/2}Ti_{1/2}$, Ga, Al) ceramics are shown in Fig.1. The main peaks in all patterns index according to a perovskite structure. However, only

compositions for which *Me* = $Mg_{2/3}Nb_{1/3}$ and Sc are free from minor peaks associated with a secondary $Bi_{22}Fe_2O_{36}$ phase (PDCF card no. is 01-084-2559). For other dopants, we propose that excess Bi arises from dopant ions that either do not or only partially occupy the B site which results in the appearance of Bi rich second phases.

To investigate the microstructure and the compositional homogeneity of the ceramics, BSE images for the polished $0.05Bi(Me)O_3$-$0.70BaTiO_3$-$0.25BiFeO_3$ ceramics were acquired (Fig. 2). For compositions with Me = $Mg_{2/3}Nb_{1/3}$ and Sc the grain size was ~5 to 10 µm and the image contrast suggested a homogeneous cation distribution, free from second phase in agreement with the XRD traces. For composition with Me = Y and $Sc_{1/2}Y_{1/2}$, the grain size was smaller, with each grain exhibiting homogeneous contrast but with a light contrast, intergranular second phase, presumably $Bi_{22}Fe_2O_{36}$ (Fig. 1) which has a larger weight average atomic number (WAA) than the perovskite matrix. For ceramics with Me = $Zn_{2/3}Nb_{1/3}$, $Zn_{1/2}Ti_{1/2}$, Ga, and Al, a much smaller average grain size is observed (<4 µm) with evidence of a core shell contrast within the grains. Regions of lighter contrast in the images are Bi-rich compared to the matrix according to energy dispersive X-ray analysis (not shown here) and assumed to be $Bi_{22}Fe_2O_{36}$, consistent with XRD data, Fig. 1. We note that there are dark precipitates present in the $BiSc_{1/2}Y_{1/2}O_3$ and $BiYO_3$ doped samples (Fig. 2a and b) which correspond, according to EDS, to an yttrium ferrite phase. We conclude therefore that Y_2O_3 does not enter the matrix. In summary, we report that only $BiScO_3$ and $BiMg_{2/3}Nb_{1/3}O_3$ doped composition are free from secondary phase and exhibit a homogeneous microstructure. All other dopants either do not enter the lattice (Y_2O_3) and/or modify the phase equilibria to promote $Bi_{22}Fe_2O_{36}$ formation. In addition, compositions with Me = $Zn_{2/3}Nb_{1/3}$, $Zn_{1/2}Ti_{1/2}$, Ga, and Al promote the formation of a two-phase perovskite matrix. Previous authors have reported that immiscibility is suppressed by quenching [22, 31].
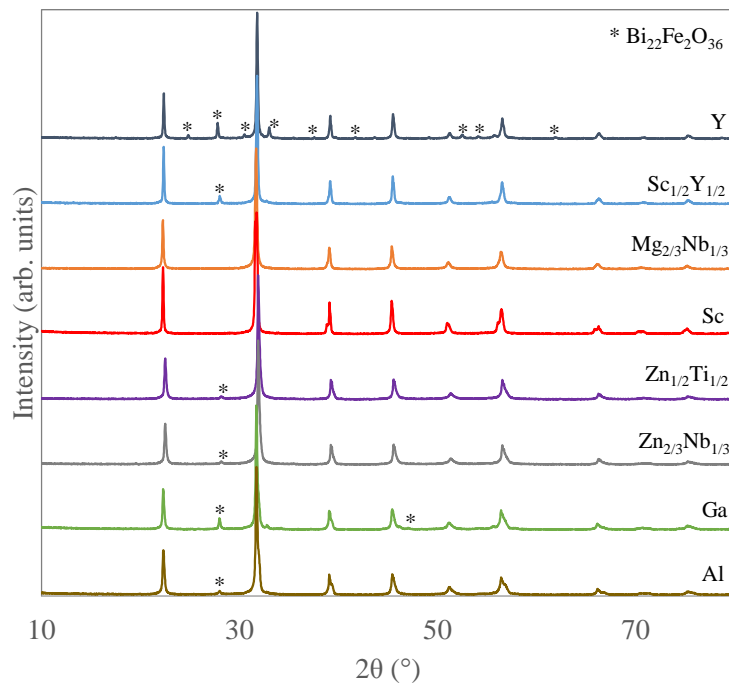
Fig. 1. XRD diffractograms of 0.05Bi(Me)O$_3$-0.70BaTiO$_3$-0.25BiFeO$_3$ (Me =Y, Sc$_{1/2}$Y$_{1/2}$, Mg$_{2/3}$Nb$_{1/3}$, Sc, Zn$_{2/3}$Nb$_{1/3}$, Zn$_{1/2}$Ti$_{1/2}$, Ga, Al) ceramics.
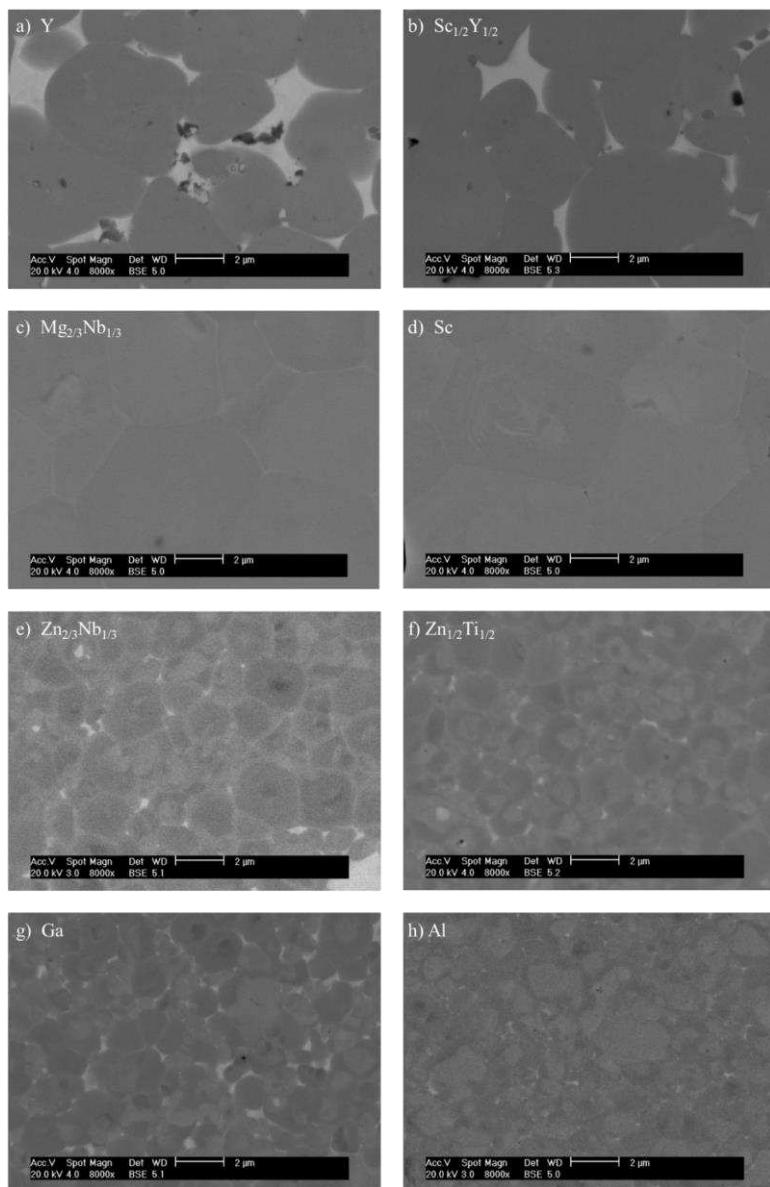
Fig. 2. BSE images of polished surface of $0.05Bi(Me)O_3$-$0.70BaTiO_3$-$0.25BiFeO_3$ ceramics. with Me = (a) Y, (b) $Sc_{1/2}Y_{1/2}$, (c) $Mg_{2/3}Nb_{1/3}$, (d) Sc, (e) $Zn_{2/3}Nb_{1/3}$, (f) $Zn_{1/2}Ti_{1/2}$, (g) Ga and (h) Al.

3.2 Temperature dependence of relative ε_r and tanδ

The temperature dependencies of ε_r and tanδ for the 0.05Bi(Me)O$_3$-0.70BaTiO$_3$-0.25BiFeO$_3$ ceramics are shown in Fig. 3(a) and 3(b) (measured at 10 kHz). All anomalies are broad and often exhibit more than one dielectric maxima but the narrowest profiles occur for compositions with Me = Y, Sc$_{1/2}$Y$_{1/2}$, Mg$_{2/3}$Nb$_{1/3}$, and Sc (Fig. 3(a)) whose matrix perovskite grains exhibit a homogenous microstructure. In contrast, compositions with Me = Zn$_{2/3}$Nb$_{1/3}$, Zn$_{1/2}$Ti$_{1/2}$, Ga, and Al, show the broadest dielectric anomalies and exhibit a two-phase perovskite core-shell matrix, attributed to immiscibility by Murakami et al [31]. The dielectric loss for Me = Y and Sc$_{1/2}$Y$_{1/2}$ (Fig. 3(b)), increases dramatically at ~100°C, consistent with the presence of a conducting grain boundary second phase (Fig. 2) with all other compositions showing a steep increase at ~ 250°C, typical of BaTiO$_3$-BiFeO$_3$ based solid solutions [31] and likely to relate to migration of oxygen vacancies (V_O).

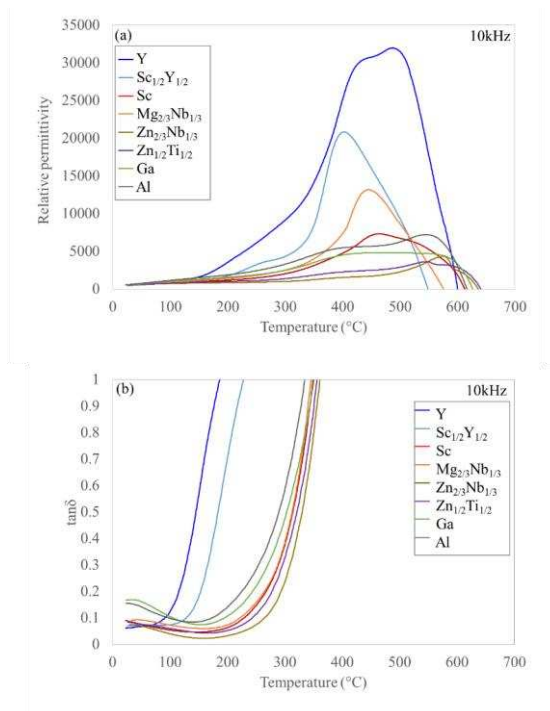Fig. 3. Temperature dependence of (a) relative permittivity and (b) dielectric loss, tanδ for 0.05Bi(Me)O$_3$-0.70BaTiO$_3$-0.25BiFeO$_3$ (Me = Y, Sc$_{1/2}$Y$_{1/2}$, Mg$_{2/3}$Nb$_{1/3}$, Sc, Zn$_{2/3}$Nb$_{1/3}$, Zn$_{1/2}$Ti$_{1/2}$, Ga, Al) ceramics.

3.3 Ferroelectric and Piezoelectric properties

PE hysteresis loops and bipolar SE curves for the $0.05Bi(Me)O_3$-$0.70BaTiO_3$-$0.25BiFeO_3$ ceramics were measured under an electric field of 7 kV/mm at room temperature (Fig. 4(a) and Fig. 4(b)). For $Me = Mg_{2/3}Nb_{1/3}$, and Sc, the PE hysteresis loops show a classic ferroelectric square loop but for Me = Y and $Sc_{1/2}Y_{1/2}$, the loops are rounded consistent with a large contribution from a space charge distribution (presumably from the Bi-rich secondary phase) within the sample and concomitant with the higher dielectric loss. Slim and mainly elliptical *PE* loops were recorded for $Me = Zn_{1/2}Ti_{1/2}$, Ga, and Al, suggesting only limited long-range ferroelectric order in these samples, consistent with the inhomogeneous matrix microstructure observed in Fig. 2.

For bipolar strain, *SE* curves for $Me = Mg_{2/3}Nb_{1/3}$, Sc, Y, and $Sc_{1/2}Y_{1/2}$ show butterfly loops typical of a long-range order ferroelectric but for $Me = Zn_{1/2}Ti_{1/2}$, Ga, and Al, the *SE* curves show a parabolic curve consistent with electrostrictive, relaxor-like materials. Compositions with $Me = Zn_{2/3}Nb_{1/3}$, exhibited near zero strain and consistent with the linear dielectric-like hysteresis loop, the significant heterogeneity in the matrix phase in Fig. 2 and the exceptionally broad dielectric anomaly in Fig. 3.

The Berlincourt (small signal) piezoelectric coefficient (d_{33}) for the $0.05Bi(Me)O_3$-$0.70BaTiO_3$-$0.25BiFeO_3$ ceramics are plotted on a graph of t versus e_n (Fig. 5). The largest d_{33} values of 145 pC/N and 146 pC/N were achieved for Me = $Mg_{2/3}Nb_{1/3}$ and Sc, consistent with the absence of secondary phase peaks in XRD traces and a homogeneous microstructure (Figs. 1 and 2), respectively. Y and $Sc_{1/2}Y_{1/2}$ exhibit smaller d_{33}, potentially due to the grain boundary secondary phase observed in BSE images (Fig. 1 and 2). Compositions with $Me = Zn_{2/3}Nb_{1/3}$, $Zn_{1/2}Ti_{1/2}$, Ga, Al exhibit a low d_{33} from 8 to 30 pC/N which we attribute to the inhomogeneous cation distribution, as evidenced by the core-shell contrast in BSE images, (Fig. 2).
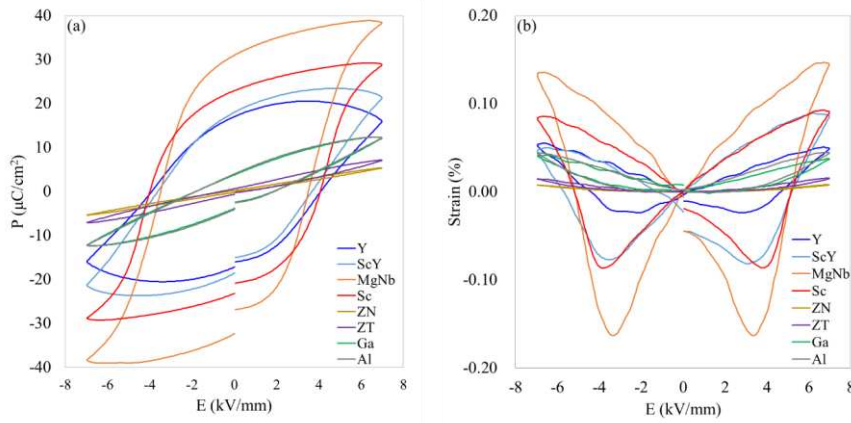
Fig. 4. (a) *PE* hysteresis loops and (b) bipolar *SE* curves for $0.05Bi(Me)O_3$-$0.70BaTiO_3$-$0.25BiFeO_3$ (*Me* = Y, $Sc_{1/2}Y_{1/2}$, $Mg_{2/3}Nb_{1/3}$, Sc, $Zn_{2/3}Nb_{1/3}$, $Zn_{1/2}Ti_{1/2}$, Ga, Al) ceramics.

3.4. Crystallochemical Considerations

Fig. 5 is a plot of e_n vs. t for $0.05Bi(Me)O_3$-$0.70BaTiO_3$-$0.25BiFeO_3$ compositions. With reference to Fig. 5 and related XRD, SEM and piezoelectric data, only $Mg_{2/3}Nb_{1/3}$ and Sc doped compositions, that lie within a narrow range of e_n vs t, successfully substitute into the BT-BF matrix without either promoting secondary phases (yttrium ferrite and $Bi_{22}Fe_2O_{36}$) or altering the matrix cation distribution to contain two immiscible perovskite phases. It is therefore no coincidence that compositions with *Me* = $Mg_{2/3}Nb_{1/3}$ and Sc reveal the optimum Berlincourt, small signal d_{33}. The effect of e_n and t on the phase assemblage has its origins in the local strain and bond strength and type induced by the substituents. Y ($R_Y = 0.9$ Å) has a large ionic radius (R) for a B-site species ($R_{Ti} = 0.605$) and it therefore does not enter the perovskite lattice but instead reacts with Fe_2O_3 to form an yttrium ferrite phase. This creates an excess of Bi_2O_3 which is observed within the microstructure as $Bi_{22}Fe_2O_{36}$ surrounding the perovskite grains, Fig. 2. Al, Ga and Zn ions have a low e_n and thus have a more covalent character to their bonding which we propose favours a stronger association with the lone pair, more covalent Bi ion within the perovskite structure. The result is an inhomogeneous distribution of cations and an immiscible two perovskite phase matrix during furnace cooling. The underlying crystal chemistry for the perovskite-perovskite phase separation is undoubtedly complex but reinterpretation of previous reports in the literature suggests that immiscibility is commonly observed but suppressed by quenching to give higher d_{33} [22]. Previous work

by the current authors also reveals regions of perovskite – perovskite immiscibility in $BiMg_{2/3}Nb_{1/3}O_3$-doped compositions as a function of x [31] but that strain is optimised in furnace cooled single-phase, chemically homogeneous compositions away from the region of immiscibility [31]. We attest therefore that, in furnace cooled samples, the superior performance of some dopants with respect to others does not particularly reflect their local defect chemistry but is rather a matter of solid solubility and the resulting phase equilibria, with the overarching maxim that for the highest strains, single phase homogeneous compositions are required. The following sections of the paper further demonstrate this premise by optimising the strain for $BiScO_3$ doped compositions, predicted based on our simple crystallochemical approach to have comparable performance to $BiMg_{2/3}Nb_{1/3}O_3$-doped compositions [31].

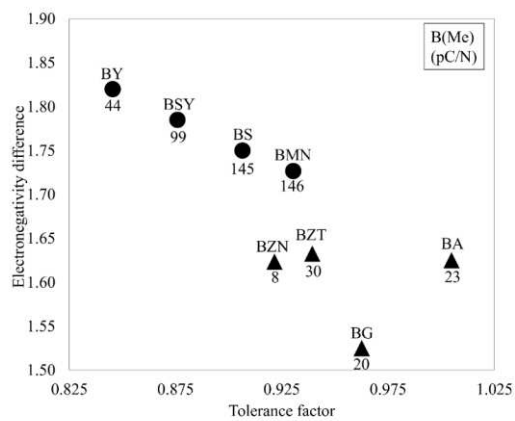Fig. 5. Piezoelectric coefficient d_{33}, tolerance factor, and electronegativity difference for $0.05Bi(Me)O_3$-$0.70BaTiO_3$-$0.25BiFeO_3$ (Me = Y (BY), $Sc_{1/2}Y_{1/2}$ (BSY), $Mg_{2/3}Nb_{1/3}$ (BMN), Sc (BS), $Zn_{2/3}Nb_{1/3}$ (BZN), $Zn_{1/2}Ti_{1/2}$ (BZT), Ga (BG), and Al (BA)) ceramics.

3.5 XRD Analysis for $0.05BiScO_3$-$(0.95-x)BaTiO_3$-$xBiFeO_3$ ceramics

To further investigate dopant effects in BT-BF systems, the relationship between the piezoelectric/ferroelectric properties and the microstructure for $0.05BiScO_3$-$(0.95-x)BaTiO_3$-$xBiFeO_3$ (BS-BT-xBF, x = 0.55, 0.60, 0.625, 0.65, and 0.70) ceramics was

investigated. Fig. 6 shows the XRD diffractograms of the BS-BT-*x*BF ceramics. On visual inspection, all XRD patterns are attributed to a single perovskite phase without any secondary phase peaks. To determine the most probable structure for each data set, Rietveld refinements were conducted and the results summarised in Table 4. All XRD patterns were refined using a combination of pseudocubic (*Pm-3m*) and rhombohedral (*R3c*) cells. For x = 0.55 to 0.65, the ratio of *R3c/Pm-3m* is dominated by *Pm-3m* but for x = 0.70 *R3c* dominates, consistent with most previous observations [35-37] although some authors refer to the presence of monoclinic or tetragonal symmetries [13, 38].
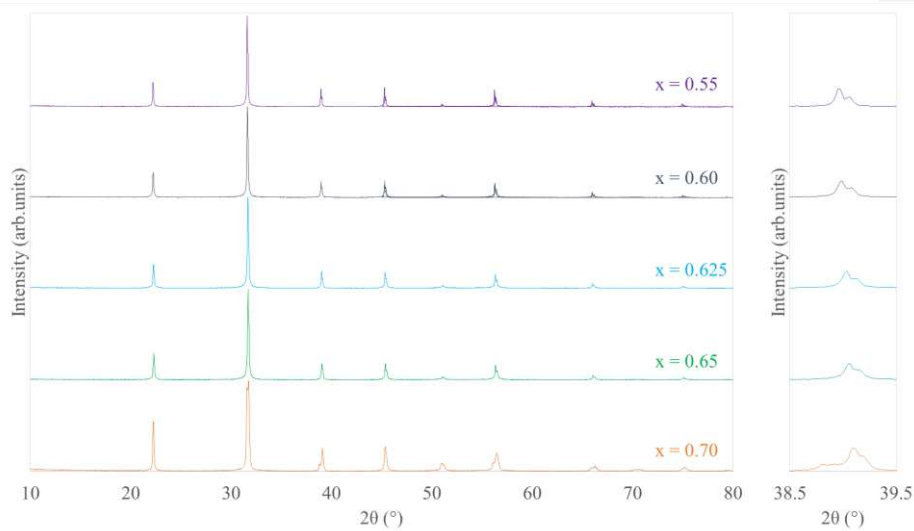

Fig. 6. Powder XRD patterns for the 0.05BiScO$_3$-(0.95-*x*)BaTiO$_3$-*x*BiFeO$_3$ ceramics measured at room temperature.

Table 4. Lattice parameters (a, b, c), fraction of phase (wt%), and fitting parameters (R_{wp}, R_p, and χ^2) for the 0.05BiScO$_3$-(0.95-x)BaTiO$_3$-(x)BiFeO$_3$ ceramics measured at room temperature.

x	Space group	Lattice parameters			Weight (%)	R-factors		
		a (Å)	b (Å)	c (Å)		R_{wp} (%)	R_p (%)	χ^2
0.55	Pm-3m	4.0059(7)	4.0059(7)	4.0059(7)	89.3	9.44	7.39	1.47
	R3c	5.6695(8)	5.6695(8)	13.8662(3)	10.7			
0.6	Pm-3m	4.0027(8)	4.0027(8)	4.0027(8)	87.1	9.74	7.73	1.64
	R3c	5.7154(6)	5.7154(6)	14.0559(6)	12.9			
0.625	Pm-3m	4.0039(4)	4.0039(4)	4.0039(4)	94.8	9.94	7.89	1.74
	R3c	5.6054(4)	5.6054(4)	13.7375(2)	5.2			
0.65	Pm-3m	4.0017(4)	4.0017(4)	4.0017(4)	91.3	10.65	8.53	2.04
	R3c	5.6089(3)	5.6089(3)	13.7112(6)	8.7			
0.7	Pm-3m	4.0006(0)	4.0006(0)	4.0006(0)	25.2	8.29	6.36	1.94
	R3c	5.6377(5)	5.6377(5)	13.9112(3)	74.8			

3.6 Microstructure of $0.05BiScO_3$-$(0.95-x)BaTiO_3$-$xBiFeO_3$ ceramics

BSE images for the $0.05BiScO_3$-$(0.95-x)BaTiO_3$-$xBiFeO_3$ are illustrated as a function of x in Fig. 7. All samples generally show uniform contrast within the grains, indicating they are compositionally homogeneous with no clear core-shell structures nor Bi rich grain boundary phases, Fig. 7 (e) ~ (h), thus confirming the prediction that Sc^{3+} readily occupies the B-site in the BT-BF system due to its 'Goldilocks' combination of ionic radius (0.745 Å) and electronegativity (1.36). However, we note that common to most BT-BMe based [31] ceramics, there are precipitates in the centre of the grains. These precipitates are thought to be residual from the early stages of reaction to form the perovskite phase during calcination [39].

To evaluate the electrical homogeneity, impedance spectroscopy (*IS*) analysis was conducted. Spectroscopic plots of *Z''* and *M''* extracted from *IS* data can be used as a simple way to qualitatively assess electrical homogeneity. Fig 8 (a-e) show *Z''* and *M''* spectroscopic plots for $0.05BiScO_3$-$(0.95-x)BaTiO_3$-$xBiFeO_3$ ceramics. For $x = 0.55$ to 0.65, data are shown for 320ºC whereas for x = 0.70, the data are shown for 243ºC to allow the *Z''* and *M''* spectra to be observed and compared with the other ceramics. All the M'' spectra show a low frequency peak with an f_{max} value that is similar to the large *Z''* peak but there are clearly further *M''* peaks at intermediate and higher frequencies. The presence of multiple *M''* peaks means all samples have two or more electrical phases present, most likely relating to either grain boundary, shell or core regions. The capacitance values calculated from the single *Z''* Debye peak measured at 320ºC for

0.05BiScO$_3$-(0.95-x)BaTiO$_3$-xBiFeO$_3$ ceramics are shown in Table 5. For x = 0.55 to 0.65, the capacitance values are ~ 1.2 to 2.8 nF/cm consistent with a grain boundary type response but the capacitance decreases to 0.29 nF/cm for x = 0.70. This capacitance decrease implies that the main electrical (conduction) path in the ceramics changes from being a grain boundary-type response to a shell-type response at x = 0.70 but further analyses are required to confirm this assignment.

The large, single Z'' Debye peak was used to calculate the total resistivity of the ceramics and the inverse of this value used to estimate the total electrical conductivity. An Arrhenius plot of the total conductivity for 0.05BiScO$_3$-(0.95-x)BaTiO$_3$-xBiFeO$_3$ ceramics is shown in Fig. 9 and the activation energy (E_a) calculated from these data are shown in Table 5. Fig. 9 shows the conductivity increases from x = 0.55 to 0.70 and Table 5 reveals all samples have approximately the same E_a of ~ 1.1 to 1.2 eV, indicating that their conduction mechanisms are similar.
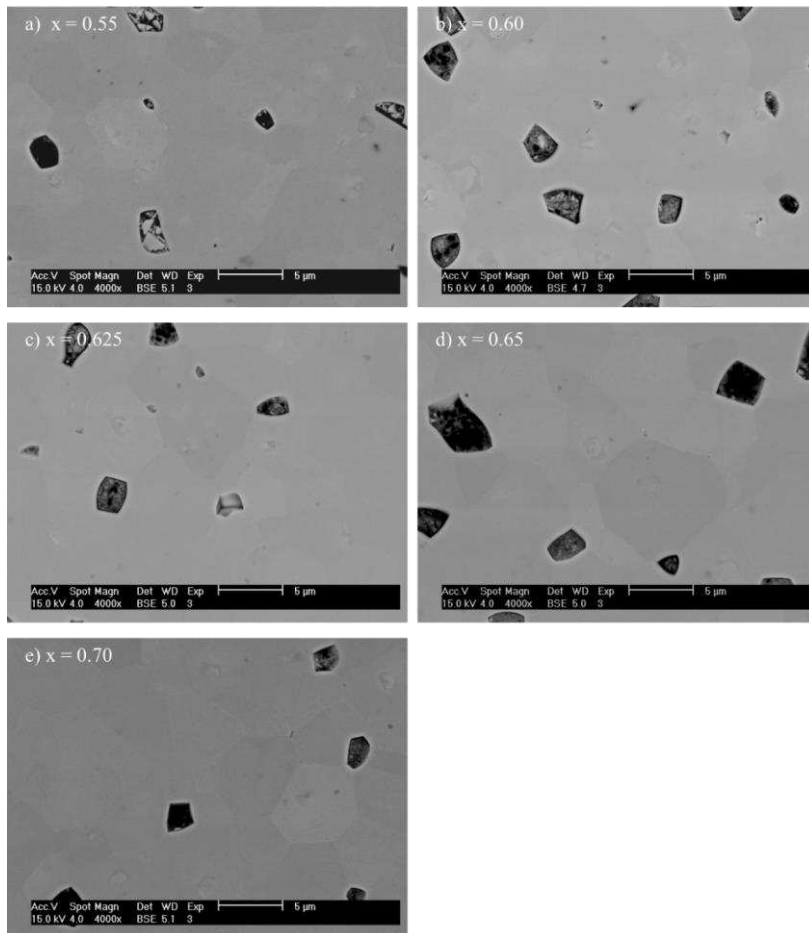
Fig. 7. BSE images of polished surface of $0.05BiScO_3$-$(0.95\text{-}x)BaTiO_3$-$x$$BiFeO_3$ ceramics with x = (a) 0.55, (b) 0.60, (c) 0.625, (d) 0.65, and (e) 0.70.
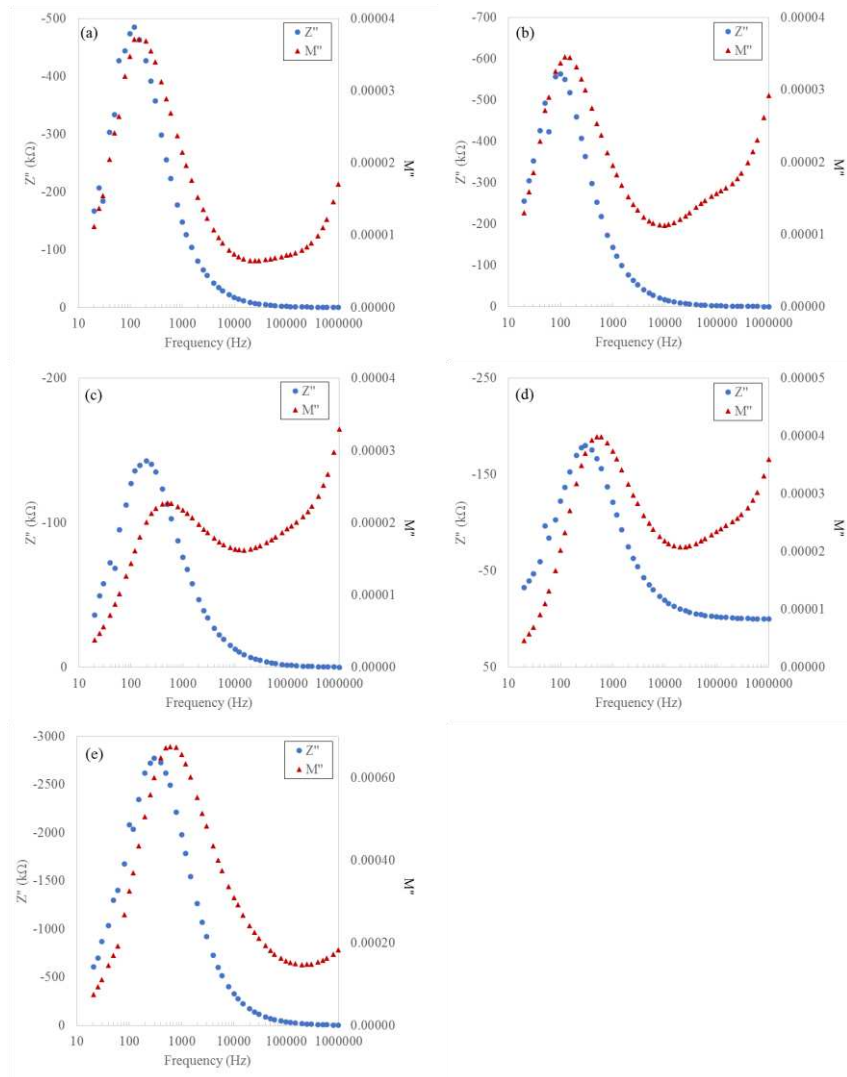
Fig. 8. Combined Z'' and M'' spectroscopic plots for 0.05BiScO$_3$-(0.95-x)BaTiO$_3$-xBiFeO$_3$ ceramics with x = (a) 0.55, (b) 0.60, (c) 0.625, (d) 0.65 measured at 320°C, and (f) 0.70 measured at 243°C.

Table 5. Capacitance measured at 320°C and activation energy for the 0.05BiScO$_3$-(0.95-x)BaTiO$_3$-xBiFeO$_3$ ceramics.

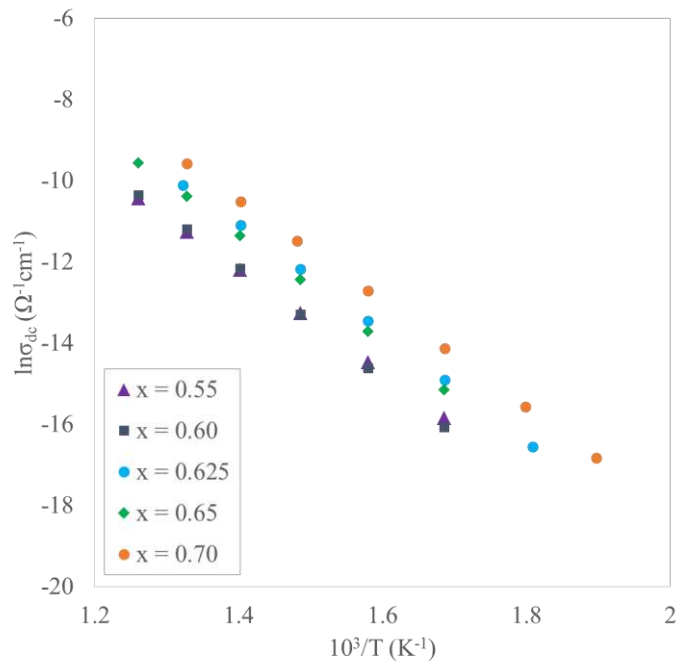| x	Capacitance at 320°C	Activation Energy
	C (nF)	E_a (eV)
0.55	1.37	1.10
0.60	1.21	1.16
0.625	2.78	1.15
0.65	1.47	1.14
0.70	0.29	1.10

Fig. 9. Arrhenius plot of electrical conductivity for the 0.05BiScO$_3$-(0.95-x)BaTiO$_3$-xBiFeO$_3$ ceramics.

3.7 Temperature dependence of ε_r and tanδ of 0.05BiScO$_3$-(0.95-x)BaTiO$_3$-xBiFeO$_3$

ceramics.

The temperature dependence of ε_r and $\tan\delta$ for the 0.05BiScO$_3$-(0.95-x)BaTiO$_3$-xBiFeO$_3$ ceramics measured at 10 kHz are shown in Fig. 10 (a) and 10 (b). For x = 0.55 (Fig. 10(a)), the dielectric anomaly is consistent with a relaxor-like transition and concomitant with the dominant pseudocubic structure refined from the XRD data. As x increases to 0.65, the dielectric anomalies become sharp and the temperature where the permittivity maximum shifts to higher temperature. For x = 0.70, there is more than one anomaly. Tanδ for all compositions at room temperature is ~0.1. In addition to tanδ and the total electrical conductivity extracted from IS data set, the detected current of all these samples was less than the current limit (0.002 mA) when poling under DC 50 kV/cm at 90 °C. These results indicate the leakage current of this system was suppressed enough to drive by AC voltage. tanδ for 0.55$\leq$$x$$\leq$0.65 does not increase significantly until > 300ºC which is encouraging for high temperature applications but for x = 0.70 the onset of the sharp increase in dielectric loss shifts to lower temperatures consistent with conductivity data obtained by impedance spectroscopy.

The frequency dependence from 1 kHz to 250 kHz of ε_r and tanδ for the 0.05BiScO$_3$-0.325BaTiO$_3$-0.625BiFeO$_3$ ceramics are shown in Fig. 11 (a) and 11 (b). With increasing frequency, the ε_r maximum shifts to higher temperature and is suppressed. The onset temperature where tanδ increases also shifts to higher temperature. It is concluded therefore that compositions with x = 0.625 are relaxor in character.
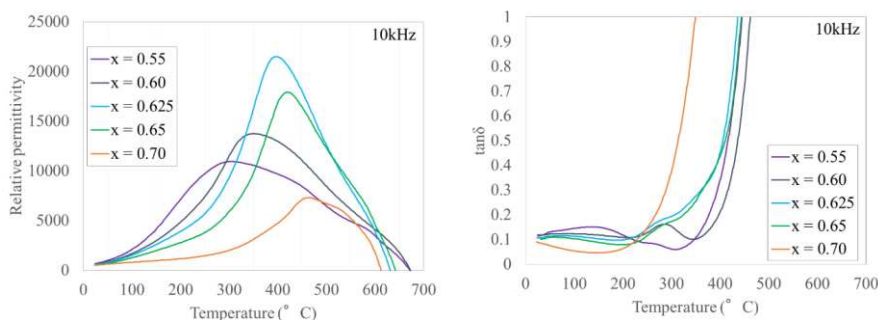

Fig. 10. Temperature dependence of (a) relative permittivity and (b) dielectric loss, tanδ for the 0.05BiScO$_3$-(0.95-x)BaTiO$_3$-xBiFeO$_3$ ceramics.
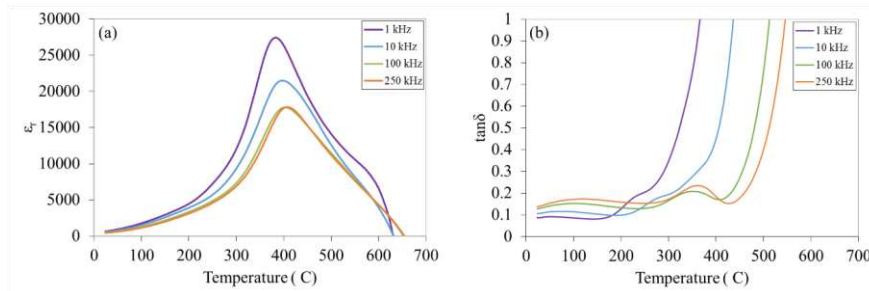
Fig. 11. Frequency dependence of (a) relative permittivity and (b) dielectric loss, tanδ vs temperature for the $0.05BiScO_3$-$0.625BaTiO_3$-$0.325BiFeO_3$ ceramics.

3.8 Ferroelectric and piezoelectric properties of $0.05BiScO_3$-$(0.95-x)BaTiO_3$-$xBiFeO_3$ ceramics

PE hysteresis loops and bipolar SE curves for $0.05BiScO_3$-$(0.95-x)BaTiO_3$-$xBiFeO_3$ ceramics were measured under an electric field of 7 kV/mm at room temperature (Fig. 12(a) and Fig. 12(b)). PE hysteresis loops show a change from a narrow loop typical of electrostrictive compositions with limited or no long-range ferroelectricity to a classic ferroelectric square loop as x increases, consistent with the increase in volume fraction of the R3c phase. A similar trend is observed for bipolar strain field measurements which transform from loops typical of dominant electrostrictive behaviour (negligible negative strain) to classic butterfly loops typical of a long-range ordered ferroelectric, consistent with the trend of the temperature dependence of relative permittivity vs temperature. Unipolar SE curves for the $0.05BiScO_3$-$(0.95-x)BaTiO_3$-$xBiFeO_3$ ceramics measured under 5 kV/mm at room temperature are shown in Fig. 13. The largest d_{33}^* (465 pm/V at $x = 0.625$), was obtained at the point of crossover from dominant relaxor, electrostrictive ($x = 0.55$) to ferroelectric behaviour ($0.60 \leq x \leq 0.70$), a trend previously observed in BMN/Nd doped BT-BF [29, 31] and Pb-free systems based on NBT and/or $(K_{0.5}Bi_{0.5})TiO_3$ (KBT) [38, 40-42]. Sc which reside well in the B site effectively moves the perovskite immiscibility region away from the 'sweet-spot' for high strain.

The temperature dependence of the unipolar SE curves for poled $0.05BiScO_3$-$(0.95-x)BaTiO_3$-$xBiFeO_3$ ($x = 0.63$) ceramics measured under an electric field of 6 kV/mm from 25 to 175ºC are shown in Fig. 14. The strain increased from ~0.27 to ~0.35% at 150 ºC and remained at ~0.35% at 175ºC, accompanied by a notable decrease in hysteresis with respect to room temperature measurements. The variation of strain (ΔS) was 31%. These

results suggest that BS-BT-BF may have the potential to operate at higher temperatures than typical for PbO-free ceramics which often have low depolarising temperatures or a decrease in piezoactivity as temperature increases [24, 42-45].
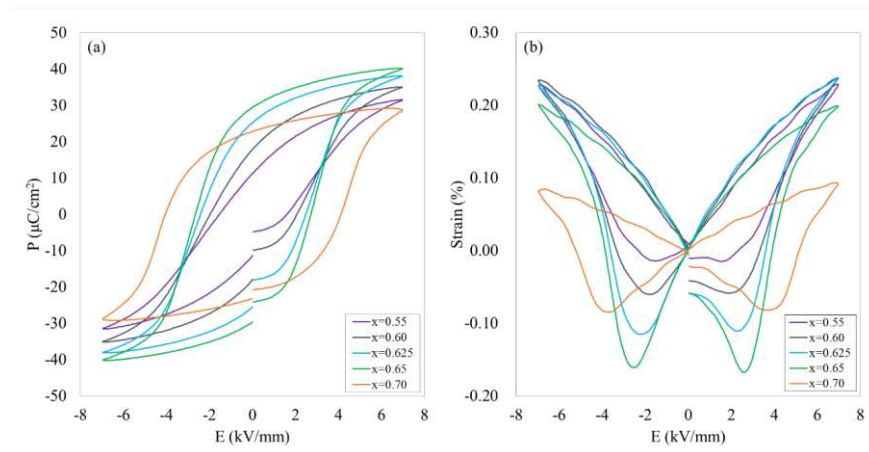

Fig. 12. (a) *PE* hysteresis loops and (b) bipolar *SE* curves for the 0.05BiScO$_3$-(0.95-*x*)BaTiO$_3$-*x*BiFeO$_3$ ceramics measured at room temperature.
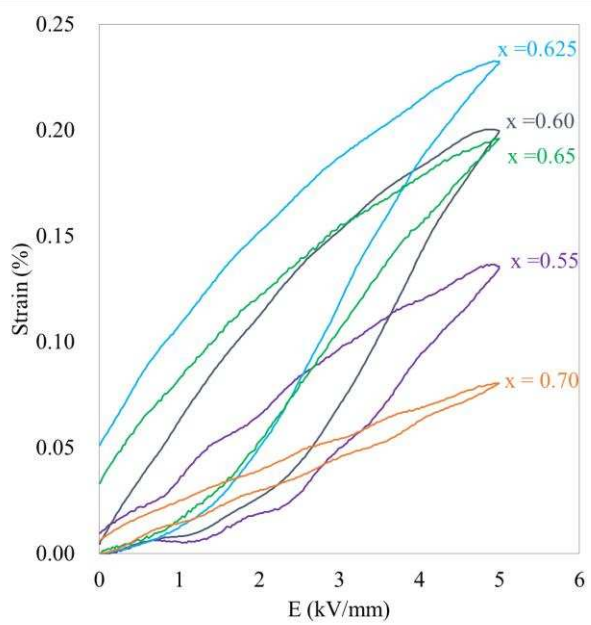
Fig. 13. Unipolar SE curves for the $0.05BiScO_3$-$(0.95-x)BaTiO_3$-$xBiFeO_3$ ceramics measured at room temperature.

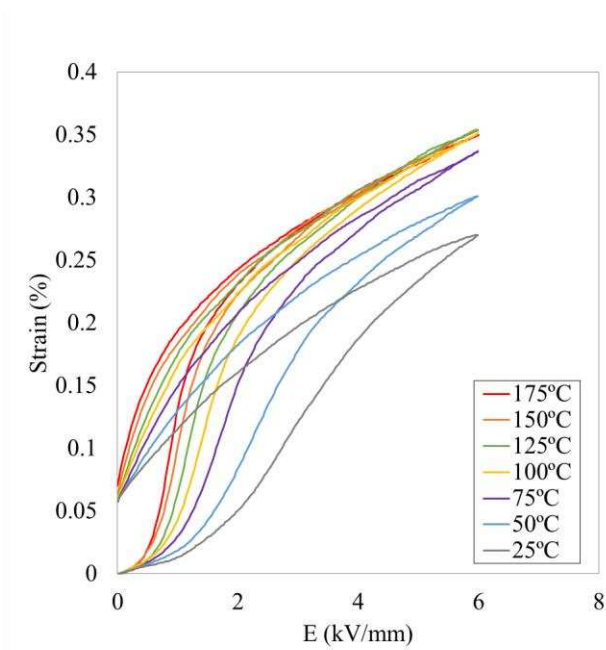Fig. 14. Temperature dependence of unipolar *SE* curves for $0.05BiScO_3$-$0.625BaTiO_3$-$0.325BiFeO_3$ ceramics measured under an electric field of 6 kV/cm at from 25 to 175°C.

4. Conclusions

The relationship between piezoelectric/ferroelectric properties and phase assemblage in $0.05Bi(Me)O_3$-$(0.95-x)BaTiO_3$-$xBiFeO_3$ ($Me = Y$, $Sc_{1/2}Y_{1/2}$, $Mg_{2/3}Nb_{1/3}$, Sc, $Zn_{2/3}Nb_{1/3}$, $Zn_{1/2}Ti_{1/2}$, Ga, Al, $x = 0.70$) was investigated as a function of e_n and t. $Mg_{2/3}Nb_{1/3}$ and Sc have similar values of t and e_n and are the only substituents that do not create secondary phases or give rise to an inhomogeneous distribution of cations. B-site ion substituents with larger radii (Y) do not enter the lattice and result in the formation of secondary phases whereas lower e_n species give rise to a two-phase inhomogeneous perovskite core-shell matrix phase (immiscibility). Optimum ferroelectric and piezoelectric properties for $x = 0.70$ were achieved for $Me = Sc$ and $Mg_{2/3}Nb_{1/3}$ which exhibit remarkably similar values of e_n and t.

As predicted, XRD patterns and BSE images of Sc-doped compositions with $0.55 \leq x \leq 0.70$ revealed a perovskite structure with no evidence of secondary phases. As x increased, the phase assemblage gradually changed from dominant pseudocubic (*Pm-3m*)

to rhombohedral (*R3c*), consistent with the PE hysteresis loops and SE curves. The largest d_{33}^{*} of ~465 pm/V was measured for $x = 0.625$ at 5 kV at the crossover from relaxor to ferroelectric behaviour. The temperature dependence for x = 0.625 showed 0.35% strain under an electric field of 6 kV/mm at 175ºC with a notable decrease in hysteresis with respect to room temperature.

References

[1] An Introduction to Piezoelectric Materials and Applications, J. Holterman & P. Groen.

[2] Y. Saito, H. Takano, T. Tani, T. Nonoyama, K. Takatori, T. Homma, T. Nagaya, and M. Nakamura, Lead-free piezoceramics, *Nature*, **432**, 84-87 (2004).

[3] R. A. Goyer, Lead Toxicity: Current concerns, *Environ Health Perspect*, **100**, 177-187 (1993).

[4] G. Lockitch, Perspectives on Lead Toxicity, *Clin Biochem,* **26**, 371-381 (1993).

[5] E. K. Akdogan, K. Kerman, M. Abazari, and A. Safari, Origin of high piezoelectric activity in ferroelectric $(K_{0.44}Na_{0.52}Li_{0.04})$-$(Nb_{0.84}Ta_{0.1}Sb_{0.06})O_3$ ceramics, *Appl. Phys. Lett.*, **92**, 112908 (2008).

[6] E. Hollenstein, D. Damjanovic, N. Setter, Temperature stability of the piezoelectric properties of Li-modified KNN ceramics, *J. Eur. Ceram. Soc.*, **27**, 4093-4097 (2007).

[7] D. Wang, F. Hussain, A. Khesro, A. Feteira, Y. Tian, Q. Zhao, I. M. Reaney, Composition and temperature dependence of structure and piezoelectricity in $(1-x)(K_{1-y}Na_y)NbO_3$-$x(Bi_{1/2}Na_{1/2})ZrO_3$ lead-free ceramics, *J. Am. Ceram. Soc.*, **100**, 627-637 (2017).

[8] R. Wang, K. Wang, F. Yao, J. Li, F. H. Schader, K. G. Webber, W. Jo, and J. Rödel, Temperature Stability of Lead-Free Niobate Piezoceramics with Engineered Morphotropic Phase Boundary, *J. Am. Ceram. Soc.*, **98** [7], 2177-2182 (2015).

[9] H. Shi, J. Chen, R. Wang, S. Dong, Full set of material constants of $(Na_{0.5}K_{0.5})NbO_3$-$BaZrO_3$-$(Bi_{0.5}Li_{0.5})TiO_3$ lead-free piezoelectric ceramics at the morphotropic phase boundary, *J. Alloys and Compounds*, **655**, 290-295 (2016).

[10] S. Zhang, A. B. Kounga, E. Aulbach, T. Granzow, W. Jo, H. Kleebe, and J. Rödel, Lead-free piezoceramics with giant strain in the system $Bi_{0.5}Na_{0.5}TiO_3$-$BaTiO_3$-$K_{0.5}Na_{0.5}NbO_3$. I. Structure and room temperature properties, *J. Appl. Phys.*, **103**, 034107 (2008).

[11] W. Liu and X. Ren, Large Piezoelectric Effect in Pb-Free Ceramics, *Phys. Rev. Lett.*, **103**, 257602 (2009).

[12] S. Murakami, T. Watanabe, T. Suzuki, T. Matsuda, and K. Miura, Effects of poling termination and aging process on piezoelectric properties of Mn-doped $BaTi_{0.96}Zr_{0.04}O_3$ ceramics, *Jpn. J. Appl. Phys.,* **54**, 10ND05 (2015).

[13] M. H. Lee, D. J. Kim, J. S. Park, S. W. Kim, T. K. Song, M. Kim, W. Kim, D. Do, and I. Jeong, High-Performance Lead-Free Piezoceramics with High Curie Temperatures, *Adv. Mater.,* **27**, 6976-6982 (2015).

[14] W. Zhou, Q. Zheng, Y. Li, Q. Li, Y. Wan, M. Wu, and D. Lin, Structure, ferroelectric, ferromagnetic, and piezoelectric properties of Al-modified $BiFeO_3$–$BaTiO_3$ multiferroic ceramics, *Phys. Status Solidi A* **212**, No. 3, 632-639 (2015).

[15] Y. Wan, Y. Li, Q. Li, W. Zhou, Q. Zheng, X. Wu, C. Xu, B. Zhu, and D. Lin, Microstructure, Ferroelectric, Piezoelectric, and Ferromagnetic Properties of Sc-Modified $BiFeO_3$–$BaTiO_3$ Multiferroic Ceramics with MnO_2 Addition, *J. Am. Ceram. Soc.*, **97** [6], 1809-1818 (2014).

[16] C. Zhou, Z. Cen, H. Yang, Q. Zhou, W. Li, C. Yuan, H. Wang, Structure,electrical properties of $Bi(Fe,Co)O_3$–$BaTiO_3$ piezoelectric ceramics with improved Curie temperature, *Physica B*, **410**, 13-16 (2013).

[17] X. Liu, Z. Xu, X. Wei, and X. Yao, Ferroelectric and Ferromagnetic Properties of $0.7BiFe_{1-x}Cr_xO_3$–$0.3BaTiO_3$ Solid Solutions, *J. Am. Ceram. Soc.*, **91** [11], 3731-3734 (2008).

[18] X. Liu, Z. Xu, S. Qu, X. Wei, J. Chen, Ferroelectric and ferromagnetic properties of Mn-doped $0.7BiFeO_3$–$0.3BaTiO_3$ solid solution, Ceram. International, **34**, 797-801 (2008).

[19] Q. Zhou, C. Zhou, H. Yang, G. Chen, W. Li, and H. Wang, Dielectric, Ferroelectric, and Piezoelectric Properties of $Bi(Ni_{1/2}Ti_{1/2})O_3$-Modified $BiFeO_3$–$BaTiO_3$ Ceramics with High Curie Temperature, *J. Am. Ceram. Soc.*, **95** [12], 3889-3893 (2012).

[20] Q. Zheng, Y. Guo, F. Le, X. Wu, D. Lin, Microstructure, ferroelectric, piezoelectric and ferromagnetic properties of $BiFeO_3$–$BaTiO_3$–$Bi(Zn_{0.5}Ti_{0.5})O_3$ lead-free multiferroic ceramics, J. Mater. Sci.: Mater Electron, **25**, 2638-2648 (2014).

[21] Z. Cen, C. Zhou, H. Yang, Q. Zhou, W. Li, C. Yan, L. Cao, J. Song, and L. Peng, Remarkably High-Temperature Stability of $Bi(Fe_{1-x}Al_x)O_3$–$BaTiO_3$

Solid Solution with Near-Zero Temperature Coefficient of Piezoelectric Properties, *J. Am. Ceram. Soc.*, **96** [7], 2252-2256 (2013).

[22] T. Zheng, Z. Jiang and J. Wu, Enhanced piezoelectricity in $(1 - x)$ $Bi_{1.05}Fe_{1-y}A_yO_3-xBaTiO_3$ lead-free ceramics: site engineering and wide phase boundary region, Dalton Trans., **45**, 11277 (2016).

[23] Q. Zheng, , L. Luo, K. H. Lam, N. Jiang, Y. Guo, and D. Lin, Enhanced ferroelectricity, piezoelectricity, and ferromagnetism in Nd-modified $BiFeO_3$-$BaTiO_3$ lead-free ceramics, *J. Appl. Phys.*, **116**, 184101 (2014).

[24] D. Wang, A. Khesro, S. Murakami, A. Feteira, Q. Zhao, I. M. Reaney, Temperature dependent, large electromechanical strain in Nd-doped $BiFeO_3$-$BaTiO_3$ lead-free ceramics, *Journal of the European Ceramic Society,* **37,** 1857–1860 (2017).

[25] X. Wu, M. Tian, T. Guo, Q. Zheng, L. Luo, D. Lin, Phase transition, dielectric, ferroelectric and ferromagnetic properties of La-doped $BiFeO_3-BaTiO_3$ multiferroic ceramics, *J. Mater. Sci.: Mater. Electron*, **26**, 978-984 (2015).

[26] R. Rai, I. Bdikin, M. A. Valente, A. L. Kholkin, Ferroelectric and ferromagnetic properties of Gd-doped $BiFeO_3-BaTiO_3$ solid solution, *Mater. Chem. and Phys.*, **119**, 539-545 (2010).

[27] D. Wang, M. Wang, F. Liu, Y. Cui, Q. Zhao, H. Sun, H. Jin, M. Cao, Sol–gel synthesis of Nd-doped $BiFeO_3$ multiferroic and its characterization, *Ceramics International*, **41**, 8768-8772 (2015).

[28] T. Zheng and J. Wu, Effects of site engineering and doped element types on piezoelectric and dielectric properties of bismuth ferrite lead-free ceramics, *J. Mater. Chem. C*, **3**, 11326-11334 (2015).

[29] D. Wang, Z. Fan, D. Zhou, A. Khesro, S. Murakami, A. Feteira, Q. Zhao, X. Tan, I. M. Reaney, Bismuth ferrite-based lead-free ceramics and multilayers with high recoverable energy density, *J. Mater. Chem. A,*, **6**, 4133-4144(2018).

[30] L. Luo, N. Jiang, X. Zou, D. Shi, T. Sun, Q. Zheng, C. Xu, K. H. Lam, and D. Lin, Phase transition, piezoelectric, and multiferroic properties of $La(Co_{0.5}Mn_{0.5})O_3$-modified $BiFeO_3-BaTiO_3$ lead-free ceramics, *Phys. Status Solidi A*, **212**, No. 9, 2012-2022 (2015).

[31] S. Murakami, D. Wang, A. Mostaed, A. Khsro, A. Feteira, D. C. Sinclair, Z. Fan, X. Tan, and I. M. Reaney, High strain (0.4%) $Bi(Mg_{2/3}Nb_{1/3})O_3$-$BaTiO_3$-$BiFeO_3$ lead-free piezoelectric ceramics and multilayers, (In press).

[32] S.J. Kuang, X.G. Tang, L.Y. Li, T.P. Jiang, and Q.X. Liu, Influence of Zr dopant on the dielectric properties and Curie temperatures of $Ba(Zr_xTi_{1-x})O_3$ ($0 \le x \le 0.12$) ceramics, *Scripta Materialia*, **61**, 68-71 (2009).

[33] T. R. Shrout and A. Halliyal, Preparation of Lead-Based Ferroelectric Relaxors for Capacitors, *Am. Ceram, Soc. Bull.*, **66**, 704 (1987).

[34] Z. C. Li and B. Bergman, Electrical properties and ageing characteristics of $BaTiO_3$ ceramics doped by single dopants, *J. Eur. Ceram. Soc.*, **25**, 441-445 (2005).

[35] M. M. Kumar, A. Srinivas, and S. V. Suryanarayana, Structure property relations in $BiFeO_3$ /$BaTiO_3$ solid solutions, *J. Appl. Phys.*, **87**, 855-862 (2000).

[36] S. O. Leontsev and R. E. Eitel, Dielectric and Piezoelectric Properties in Mn-Modified (1-x)$BiFeO_3$–x$BaTiO_3$ Ceramics, *J. Am. Ceram. Soc.*, **92**, 2957-2961 (2009).

[37] H. Zhang, W. Jo, K. Wang, K. G. Webber, Compositional dependence of dielectric and ferroelectric properties in $BiFeO_3$–$BaTiO_3$ solid solutions, *Ceram. International*, **40**, 4659-4765 (2014).

[38] R. A. M. Gotardo, D. S. F. Viana, M. Olzon-Dionysio, S.D. Souza, D. Garcia, J. A. Eiras, M. F. S. Alves, L. F. Cótica, I. A. Santos, and A. A. Coelho, Ferroic states and phase coexistence in $BiFeO_3$-$BaTiO_3$ solid solutions, *J. Appl. Phys.*, **112**, 104112 (2012).

[39] M. A. Beuerlein, N. Kumar, T. Usher, H. J. Brown-Shaklee, N. Raengthon, I. M. Reaney, D. P. Cann, J. L. Jones, and G. L. Brennecka, Current Understanding of Structure–Processing–Property Relationships in $BaTiO_3$–Bi(M)O_3 Dielectrics, *J. Am. Ceram. Soc.*, **99**, 2849–2870 (2016).

[40] S. Zhang, A. B. Kounga, and E. Aulbach H. Ehrenberg J. Rödel, Giant strain in lead-free piezoceramics $Bi_{0.5}Na_{0.5}TiO_3$-$BaTiO_3$-$K_{0.5}Na_{0.5}NbO_3$, *Appl. Phys. Lett.*, **91**, 112906 (2007).

[41] E. A. Patterson, D. P. Cann, J. Pokorny, and I. M. Reaney, Electromechanical strain in $Bi(Zn_{1/2}Ti_{1/2})O_3$–$(Bi_{1/2}Na_{1/2})TiO_3$–$(Bi_{1/2}K_{1/2})TiO_3$ solid solutions, *J. Appl. Phys.*, 111, 094105 (2012).

[42] X. Liu, J. Zhai, B. Shen, F. Li, Y. Zhang, P. Li, B. Liu, Electric-field-temperature phase diagram and electromechanical properties in lead-free $(Na_{0.5}Bi_{0.5})TiO_3$-based incipient piezoelectric ceramics, *Journal of the European Ceramic Society,* **37,** 1437–1447 (2017).

[43] A. Khesro, D. Wang, F. Hussain, D. C. Sinclair, A. Feteira, and I. M. Reaney, Temperature stable and fatigue resistant lead-free ceramics for actuators, *Appl. Phys. Lett.,* **109**, 142907 (2016).

[44] Y. Ehara, N. Novak, A. Ayrikyan, P. T. Geiger, and K. G. Webber, Dielectric, Phase transformation induced by electric field and mechanical stress in Mn-doped $(Bi_{1/2}Na_{1/2})TiO_3$-$(Bi_{1/2}K_{1/2})TiO_3$ ceramics, *J. Appl. Phys.*, **120**, 174103 (2016).

[45] L. Li, J. Hao, R. Chu, Z. Xu, W. Li, J. Du, P. Fu, Ferroelectric and field-induced strain response of lead-free (Fe,Sb)-modified $(Bi_{0.5}Na_{0.5})_{0.935}Ba_{0.065}TiO_3$ ceramics, *Ceramics International,* **42,** 9419–9425 (2016).